九州大学学術情報リポジトリ
Kyushu University Institutional Repository

# Mapping of Energy Cascade in the Developing Region of a Turbulent Round Jet

Mohd Rusdy Yaacob
Faculty of Electrical Engineering, Universiti Teknikal Malaysia Melaka

Buchhave, Preben
Intarsia Optics

Clara Marika Velte
Department of Mechanical Engineering, Technical University of Denmark

https://doi.org/10.5109/4480720

出版情報：Evergreen. 8 (2), pp.379-396, 2021-06. Transdisciplinary Research and Education Center for Green Technologies, Kyushu University
バージョン：
権利関係：Creative Commons Attribution-NonCommercial 4.0 International

KYUSHU UNIVERSITY

EVERGREEN Joint Journal of Novel Carbon Resource Sciences & Green Asia Strategy, Vol. 08, Issue 02, pp379-396, June 2021

# Mapping of Energy Cascade in the Developing Region of a Turbulent Round Jet

Mohd Rusdy Yaacob[1,*], Preben Buchhave[2], Clara Marika Velte[3]
[1]Faculty of Electrical Engineering, Universiti Teknikal Malaysia Melaka, Hang Tuah Jaya,
76100 Durian Tunggal, Melaka, Malaysia
[2]Intarsia Optics, Sønderskovvej 3, 3460 Birkerød, Denmark
[3]Department of Mechanical Engineering, Technical University of Denmark, Nils Koppels Alle, Building 403,
2800 Kgs. Lyngby, Denmark

*Author to whom correspondence should be addressed:
E-mail: rusdy@utem.edu.my

(Received January 7, 2021; Revised April 26, 2021; accepted April 26, 2021).

**Abstract**: Due to practical limitations for conducting measurements in the most interesting, yet difficult flow regions with high shear and turbulence intensities, developing turbulence has been under-explored. These limitations have impaired the ability to properly test the critical assumptions of existing turbulence theory. This paper describes experimental works for acquiring velocity data points and resolving higher order moments of velocities, which may reveal interesting non-equilibrium features of the flow. The measurements presented herein provide a uniquely accurate measurement database of a canonical high shear and high intensity turbulent flow that can serve as a baseline for further theoretical and modelling developments.

Keywords: Turbulent round jet; developing region; spatial energy spectra; structure functions; dissipation

## 1. Introduction

Turbulence study is essential from which all the important findings are notably viable in various engineering applications involving the air jet[1], air flow distribution[2] as well as in wind turbine[3][4]. The central , yet somewhat implicit, assumption of the Kolmogorov theory of turbulence is that of the universal equilibrium of the intermediate and smallest scales[5][6][7]. Of particular interest are the mechanisms that determine how energy is cascaded from large to small scales and, consequently, the mechanisms setting the level of dissipation, which is central to turbulence theory and modelling. According to Richardson's energy cascade, turbulent kinetic energy is assumed to be transferred primarily by interaction between adjacent scales (so-called local interactions)[8]. Recent evidence, however, suggests that the interactions are likely to be more complex, which demands further investigation. Tsinober[9] has challenged the misconception that large scales and small-intermediate scales are decoupled and non-interacting. Furthermore, studies like Anselmet, Antonia, and Danaila[10] have introduced the non-universality of small scale properties due to stream-wise inhomogeneity, by considering the small-scale intermittency of energy transfer, which contradicts the Richardson-Kolmogorov theory. In fact, Kolmogorov[11] himself has even suggested corrections to the K41 law for intermittency in the inertial subrange.

Significant challenges to the classical theory have continued to emerge: For example, studies conducted by[12] investigating spectrally the discrepancy between the asymptotic predictions of Kolmogorov's -5/3 power law and actual measured phenomena in the case of decaying grid turbulence flow. They also found non-negligible inhomogeneity in the same flow, which suggested a future experiment to be done with a turbulent round jet. As a prominent example, the work by Elaine Oran and her group has provided significant inspiration to evolving non-equilibrium turbulence[13]. These works have motivated us to further investigate the developing region and possible non-equilibrium behavior of the stationary turbulent round jet, which has been proven to display good agreement with Kolmogorov's theory on average in the fully developed (equilibrium) region[14].

The complex conditions in the developing region of a jet, such as high turbulence intensities, significant shear and inhomogeneity, considerably limit the choice of usable (accurate) measurement techniques. The laser Doppler anemometer (LDA) is the only known instrument that can accurately measure within this region with sufficient dynamic range, without disturbing the flow and successfully distinguishing the spatial velocity components from each other, even at high turbulence intensities[15]. Unfortunately, commercial systems have been proven to produce unreliable outputs necessary for producing unbiased statistics[16]. That is why we have developed a novel and state-of-the-art LDA system[17] to overcome the known limitations of commercially available systems[16]. This software-driven system has also been validated through series of measurements using both side scattering[18] and forward scattering configurations[19]. The (statistically averaged) results from both have shown good agreement with Kolmogorov's local equilibrium assumption in the equilibrium (fully developed) region of the jet, while revealing promising new features in the non-equilibrium counterpart, which will be emphasized further in this paper. This self-developed system was therefore used to map the developing region (downstream and radial traverses) of the round turbulent jet up to the point where the second-order moments of the velocities are known to be fully developed. Polynomials' coefficients of most of the measurement profiles are also provided for turbulence modelers to improve their computational models for non-equilibrium turbulence, for example in the flow simulations of the wind tunnel[20] and wind turbine [21][22].

The following section briefly explains the LDA experimental set-up and how the static moments were computed. In Section 3, the development of mean velocities, variance, turbulence intensities, spatial energy spectra, structure functions and mean energy dissipation profiles are reported and discussed.

## 2. Methodology

### 2.1 Flow generating facility

The same setup as in[19] was used, which is a jet generator box fabricated in the DTU workshop and replicates the one used in[23][16]. The jet box is fitted with an outer nozzle of 10 mm-diameter and contraction ratio of 3.2:1 and supplied with pressurized air and seeding particles (glycerine). It was mounted on a two-axis traverse and placed in a large tent (3 x 5.8 x 3.1 m$^3$) to minimize light pollution, external flow disturbances and particles leakage to surroundings. The jet pressure was set to provide a jet exit velocity = 35 m/s and corresponding Re = 22000, while the seeding pressure was adjusted to be around 1.4 bar to give an optimum data rate.

### 2.2 Laser Doppler anemometry system settings

The diameter of the (approximately spherical) measurement volume is around 90 µm and the average data rate was approximately 25000 s$^{-1}$ at $x/D$=30, centreline. Suitable sampling rates were chosen based on the Nyquist condition in order to avoid erroneous frequency measurement; either 25 MHz or 12.5 MHz, which resulted in a total number of samples of 25 million. To increase the signal-to-noise ratio, the photodetector was mounted in 45° forward scattering (see Fig. 1), which naturally puts high demands on accurate and robust optical alignment.

Measurements of the axial (streamwise) component of velocities spanning from downstream positions $x/D$=5 up to $x/D$=30 were acquired at different radial points as illustrated in Fig. 2. This measurement scheme was determined from the mapping obtained during the preliminary experiment[24], which was performed earlier to capture the regions where the turbulence development was most marked. The high level of fluctuations observed from that experiment has also highlighted the need to use a suitable optical frequency shift in order to obtain unbiased velocity measurement especially in the shear layers and the outer region of the jet. To do this, the beams were directed through a dual Bragg cell, which shifted one of the beams by a known frequency, i.e., 40MHz while the other shifted the frequency of the other beam by 37MHz, which resulted in an effective shift of 3MHz.

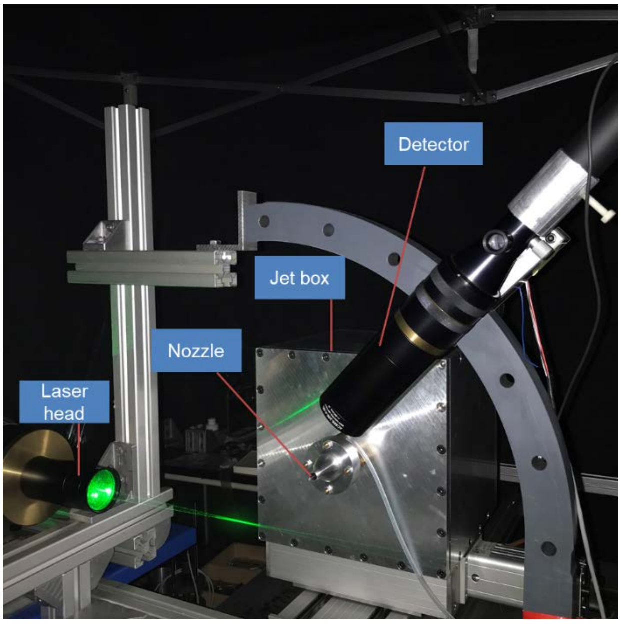

**Fig. 1:** In-house LDA system showing jet exit with the detector (lens focal length, *f*=200mm) positioned in 45° forward scattering

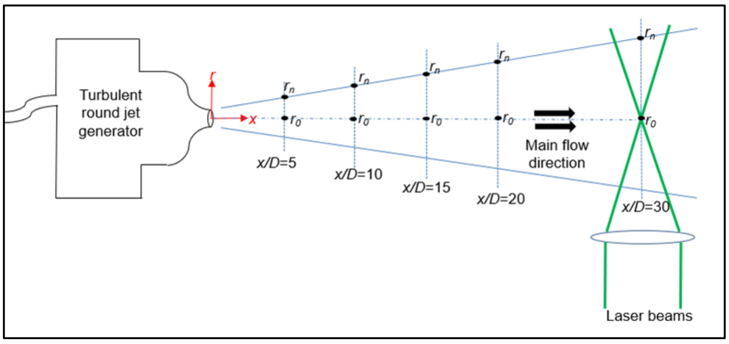

**Fig. 2:** Top view sketch of the setup showing the measurement point distribution in the downstream *x*-direction and in the radial, *r*-direction.

### 2.3 Velocity static moments

Signals obtained from the measurements were digitized, saved and processed using our own, recently developed, in-house software17), which provides the arrival time, residence time and instantaneous streamwise velocity of each particle. The mean velocity, $\bar{u}$ and variance, $\overline{u^2}$ are calculated using Eq. 1 and Eq. 2, respectively, which employed residence time-weighting for unbiased temporal statistics, as proposed by:

$$\bar{u} = \frac{\sum_{n=0}^{N-1} u_i(t_n)\Delta t_n}{\sum_{n=0}^{N-1} \Delta t_n} \tag{1}$$

$$\overline{u^2} = \frac{\sum_{n=0}^{N-1} [u_i(t_n) - \bar{u}_i]^2 \Delta t_n}{\sum_{n=0}^{N-1} \Delta t_n} \tag{2}$$

where $\Delta t_n$ is the residence time for the $n^{th}$ realization. This scheme has been shown analytically, from first principles, as well as experimentally18), to provide non-biased statistics of the LDA burst signal.

### 2.4 Temporal-to-spatial mapping

To obtain a faithful representation of the energy content of the spatial structures, the mapping from temporal to spatial records was performed based on the convection record principle16), where the instantaneous velocity magnitude has been employed rather than the average streamwise velocity as proposed by Taylor's hypothesis. Turbulent flow measurement records were thereby converted from temporal to spatial domain, bypassing the adverse fluctuating convection velocity effect25). This transformation is given by Eq. 3:

$$s(t) = \int_0^t |\bar{u}(x_0, t')| dt' \tag{3}$$

where $s$ is the scalar length of accumulated convection elements for fluid passing through the spatial record volume, $\bar{u}$ is the instantaneous velocity vector at an instantaneous time, $t'$, and $x_0$ is the location of the fixed measuring volume. Note that this method requires the flow to be stationary at the measurement point in order to acquire a homogeneous spatial record, which can be used to compute sensible static statistical quantities.

### 2.5 Computation of spatial structure functions

The classical second- and third-order spatial structure functions, respectively, are defined as:

$$S_2(\ell_x) = \langle \left(\bar{u}_x(x + \ell_x, t) - \bar{u}_x(x, t)\right)^2 \rangle \tag{4}$$

$$S_3(\ell_x) = \langle \left(\bar{u}_x(x + \ell_x, t) - \bar{u}_x(x, t)\right)^3 \rangle \tag{5}$$

where $\bar{u}_x$ is the streamwise velocity and $\ell_x$ is the spatial separation along the $x$-axis. The brackets < > denote ensemble averaging.

Since the convection record18) is employed herein to obtain a homogeneous spatial record, in a stationary random velocity signal in a single measurement point, the second- and third-order structure functions, respectively, can be expressed as:

$$S_2(\ell_s) = \langle \left(\bar{u}_x(s + \ell_s) - \bar{u}_x(s)\right)^2 \rangle \tag{6}$$

$$S_3(\ell_s) = \langle \left(\bar{u}_x(s + \ell_s) - \bar{u}_x(s)\right)^3 \rangle \tag{7}$$

where $\ell_s$ is the spatial separation along the $s$-record. Note that the < > brackets again denote ensemble averaging, but herein effectively reduces to a time average (or a spatial average along the mapped spatial coordinate $s$). The second- and third-order structure functions are related for locally isotropic turbulence in an incompressible fluid26):

$$\left(\frac{d}{d\ell_s} + \frac{4}{\ell_s}\right)\left(6\nu \frac{dS_2}{d\ell_s} - S_3\right) = 4\varepsilon \tag{8}$$

where $\nu$ is the kinematic viscosity and ε is the mean energy dissipation rate per unit mass. Based on the second hypothesis of similarity for large $\ell_s$5), the second-order structure function from Eq. 6 can be reduced to:

$$S_2(\ell_s) \sim C\varepsilon^{2/3}{\ell_s}^{2/3} \tag{9}$$

Meanwhile with the conditions where $\frac{dS_2(0)}{d\ell_s} = S_3(0) = 0$ and for large $\ell_s$, the third-order structure functions from Eq. 7 can be reduced to:

$$S_3(\ell_s) \sim -\frac{4}{5}\varepsilon\ell_s \tag{10}$$

The size of the measurement volume was firstly estimated prior to the conversion process by equating the spatial record obtained from the convection record method with the one obtained by Taylor’s frozen turbulence hypothesis. The actual size of the measurement volume could be found if the spatial records obtained from both methods were equal to each other, as long as the gain used throughout the measurement is constant. This comparison was made for the record at the jet centreline for each downstream position, where turbulence intensities are at the lowest and where Taylor’s hypothesis is known to be valid to a good approximation18).

### 2.6 Computation of Kolmogorov time and length scales

The Kolmogorov time, $\tau_{Kol}$ and length scales, $\eta_{Kol}$ are herein computed directly using Eq. 11 and Eq. 12 respectively:

$$\boldsymbol{\tau_{Kol}} = \left(\frac{\nu}{\varepsilon}\right)^{1/2} \tag{11}$$

$$\boldsymbol{\eta_{Kol}} = \left(\frac{\nu^3}{\varepsilon}\right)^{1/4} \tag{12}$$

where ε is the mean energy dissipation rate per unit mass and ν is the kinematic viscosity of the working fluid.

## 3. Results

### 3.1 Velocity static moments

Fig. 3 shows the radial profiles of measured mean velocity, variance and turbulence intensity, respectively, at each measured downstream position throughout the developing region. As expected from the spreading of the jet, the mean velocity profiles spread out and taper with increasing downstream position. Meanwhile, the variance peaks in the production intensive shear layer, as expected, and spreads and tapers with downstream development. Due to the developments from a laminar jet core, the turbulence intensities are significantly lower at *x/D*=5 compared to the other downstream positions along the jet centreline. These measurements are by nature very challenging especially in the outer part of the jet due to limitation in dynamic range with common measurement techniques. For instance, hot wire anemometry (HWA) may offer a high dynamic range but it cannot accurately represent high turbulence intensities while particle image velocimetry (PIV) could not measure small velocity changes as accurately due to its lower dynamic range.

The radial profiles of turbulence intensity (except for *x/D*=5) were also replotted in the search of potential collapses by normalizing the radial distance, r with the downstream distance, x as depicted in Fig. 4(a). In general, higher turbulence intensities are observed in the shear layer compared to the centreline due to the highly energetic large turbulent structures generated by the mixing layer. The profiles for the more downstream positions (x/D=15, 20 and 30) are observed to collapse, which agrees with the established finding obtained by [15], established in the fully developed region. In our case, it is also surprising to observe that even the profile for *x/D*=10 nearly collapses with the more downstream positions throughout the developing region. This behaviour should therefore be predicted on the radial profiles of mean velocity and variance too since turbulence intensity is comprised of these two parameters. The prediction agrees with the results plotted in Fig. 4(b) and nearly in Fig. 4(c), where the data at each measurement point were normalized by the centreline mean velocity, $U_C$, as previously implemented by [15], and the centreline variance, $\overline{u^2}_C$, respectively. Except for *x/D*=10, the radial profiles of the normalized mean velocity collapse convincingly, which is in a good agreement with the results obtained by [27] where the collapse occurred at *x/D*= 15, 18 and 20. Radial profiles of the normalized velocity variance at *x/D*=10 is also the most unlikely to collapse while for the rest, the collapse is more dominant at larger radial positions.

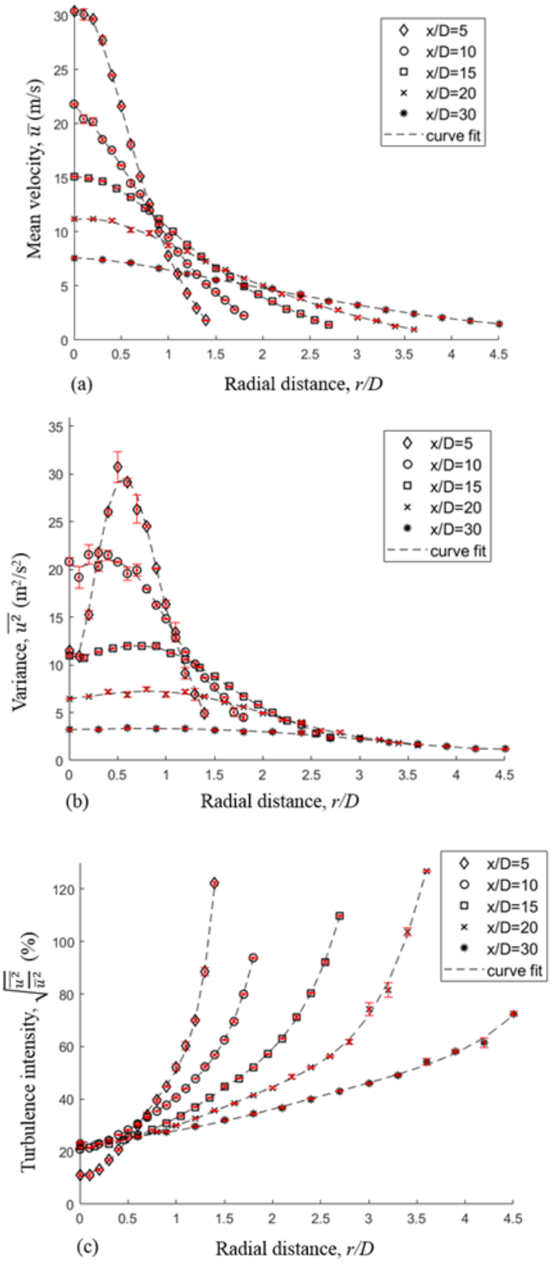

**Fig. 3:** Radial profiles of (a) mean velocity, (b) variance, (c) turbulence intensity at *x/D* = 5, 10, 15, 20 and 30 with 5th order polynomial curve fits and error bars (in *red*). Coefficients for the polynomials are listed in Appendix I (also for the following figures).

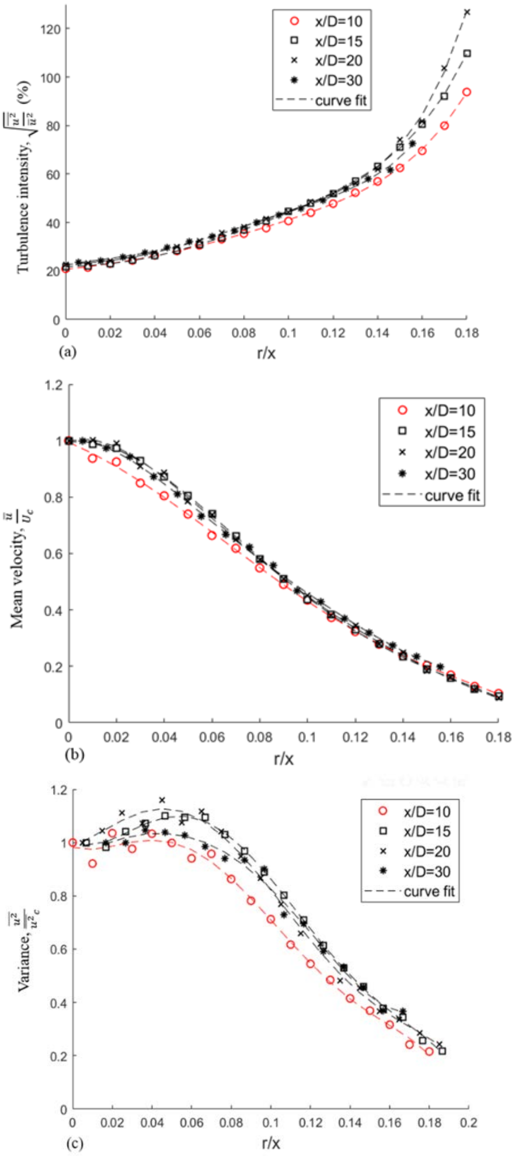

**Fig. 4:** Radial profiles of normalized (a) turbulence intensity (b) mean velocity, (c) variance at *x/D* = 10, 15, 20 and 30 with 5th order polynomial curve fits

### 3.2 Spatial kinetic energy spectra

Resulting spatial spectra for each measured centreline position downstream are shown in Fig. 5. Each spectrum is normalized to 1 (also for the following figures) in the low wave number asymptote so that a fair comparison can be made in terms of the spectrum's shape and slope with respect to Kolmogorov's -5/3 law. With downstream distance *x*, the turbulence is seen to rapidly develop from a clear steep deviation from the -5/3 slope to a state approaching -5/3 in the fully developed region with an increasingly (spectrally) wider -5/3 slope region. At the most upstream positions, the -5/3 slope is, at best, only locally tangent to any of the measured spectra.

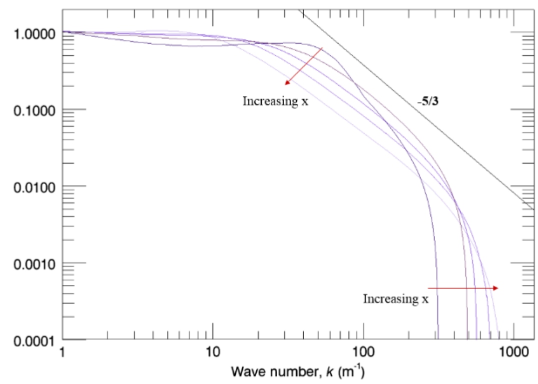

**Fig. 5:** Downstream development of spatial turbulent kinetic energy (convection record) spectra along the jet centreline ($r$ = 0). Each spectrum is normalized to 1 in the low wave number asymptote for a more clear comparison in terms of its shape and slope with respect to Kolmogorov's -5/3 law. From *heavy to light purple*: x/D = 5, 10, 15, 20, 30.

The spectrum for the position closest to the jet exit, i.e. *x/D*=5, displays a 'bump', which is expected to result from vortex rings emerging periodically due to the Kelvin Helmholtz shear layer instability[28)]. The vortex rings then become unstable as they are convected downstream, explaining the gradual disappearance of the bump on the spectra for the positions away from the jet exit and also from the jet centreline as demonstrated in Fig. 6. It shows that the effect of the Kelvin Helmholtz instability does not remain dominating in the spectrum for a very long time and is not only local in the downstream direction, but in the radial direction as well. From the temporal energy spectrum plotted in the frequency domain for *x/D*=5, centreline, the peak of the bump was found to be at around 800 Hz, which corresponded to a Strouhal number of 0.25. This value is in good agreement with the range of the preferred mode a when operating an axisymmetric turbulent jet according to [29)], i.e., from 0.24 to 0.64.

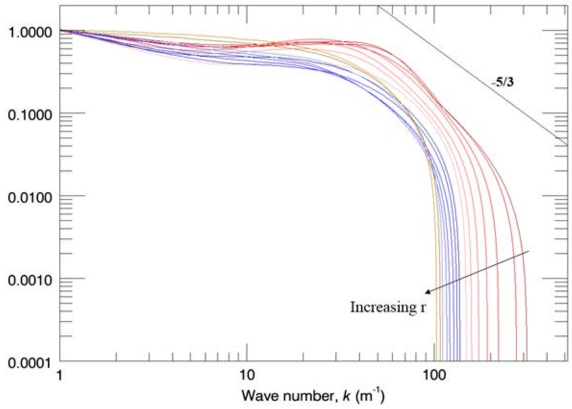

**Fig. 6:** Radial development of spatial turbulent kinetic energy (convection record) spectra at *x/D*=5. Each spectrum is normalized to 1 in the low wave number asymptote for a more clear comparison in terms of its shape and slope with respect to Kolmogorov's -5/3 law. From *heavy to light red*: *r/D* = 0, 0.1, 0.2, 0.3, 0.4, 0.5, 0.6. From *heavy to light blue*: *r/D* = 0.7, 0.8, 0.9, 1, 1.1, 1.2. From *heavy to light brown*: *r/D* = 1.3, 1.4.

Meanwhile, spectra for all measured radial distances from the jet centreline, along the remaining measured downstream positions are shown in Fig. 7(a) – (d). A clear shift from high to lower wave numbers with increasing radial distance can be observed in the developing region, so the smallest scales are larger away from the jet centreline. The shape of the spectra also varies somewhat with radial position, in particular in the more upstream measurement positions, showing that the distribution of spatial velocity structures varies with radial distance from the centreline and also with downstream direction. In the fully developed region, i.e., at *x/D*=30, the spectra convincingly collapse (to within measurement error), indicating that energy is distributed nearly equally across all the scales independent of radial position from the centreline[18]. This indicates that the second-order moments of turbulence may finally have reached a state of self-similarity in the far field of the jet.

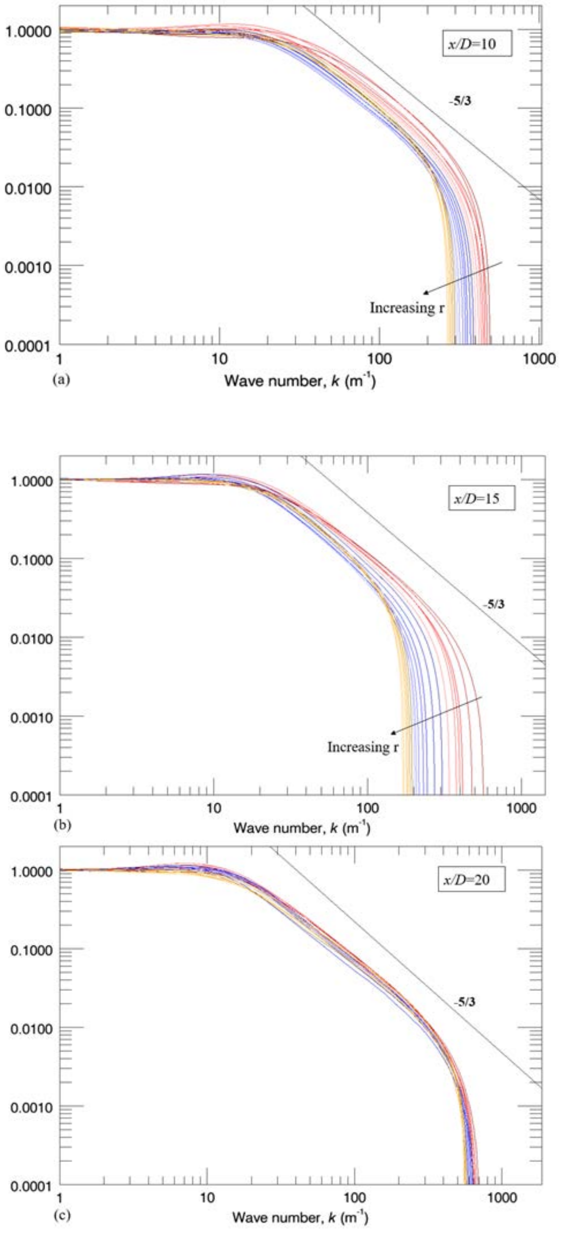

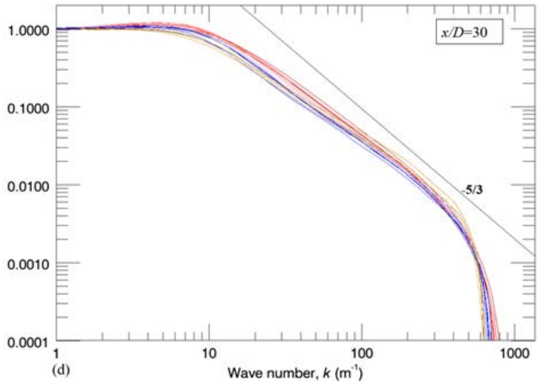

**Fig. 7:** Radial development of spatial turbulent kinetic energy (convection record) spectra at: (a) *x/D*=10. From *heavy to light red*: *r/D* = 0, 0.1, 0.2, 0.3, 0.4, 0.5, 0.6. From *heavy to light blue*: *r/D* = 0.7, 0.8, 0.9, 1, 1.1, 1.2, 1.3. From *heavy to light brown*: *r/D* = 1.4, 1.5, 1.6, 1.7, 1.8. (b) x/D=15. From *heavy to light red*: *r/D* = 0, 0.15, 0.3, 0.45, 0.6, 0.75. From *heavy to light blue*: *r/D* = 0.9, 1.05, 1.2, 1.35, 1.5, 1.65, 1.8. From *heavy to light brown*: *r/D* = 1.95, 2.1, 2.25, 2.4, 2.55, 2.7. (c) *x/D*=20. From *heavy to light red*: *r/D* = 0, 0.2, 0.4, 0.6, 0.8, 1. From *heavy to light blue*: *r/D* = 1.2, 1.4, 1.6, 1.8, 2, 2.2, 2.4. From *heavy to light brown*: *r/D* = 2.6, 2.8, 3, 3.2, 3.4, 3.6. (d) *x/D*=30. From *heavy to light red*: *r/D* = 0, 0.3, 0.6, 0.9, 1.2, 1.5. From *heavy to light blue*: *r/D* = 1.8, 2.1, 2.4, 2.7, 3, 3.3, 3.6. From *heavy to light brown*: *r/D* = 3.9, 4.2, 4.5. Each spectrum is normalized to 1 in the low wave number asymptote for a more clear comparison in terms of its shape and slope with respect to Kolmogorov's -5/3 law.

Also, in the most downstream measured position, i.e., *x/D*=30, a clear -5/3 slope across a significant range is finally displayed. It is only when we have a clear -5/3 slope that we can argue for the existence of an inertial subrange with a constant spectral flux, which makes the local equilibrium model of Kolmogorov and Batchelor valid. On a separate note, the tendency for the spectra to follow -5/3 can already be well observed at *x/D*=20 but just across a smaller wavenumber-range.

### 3.3 Spatial second-order structure function

Fig. 8 shows the (convection record based) spatial second-order structure functions along the centreline for the various measured downstream positions. Each curve is shifted in the vertical direction (also for the following figures) at the small separation region to clearly differentiate the shape of the scales development. The range within which each curve well approximates the 2/3 slope is observed to become larger in the downstream direction. The greatest tendency to follow the 2/3 slope is at *x/D*=30 (equilibrium), as expected and also obtained in [12)30)], while a significant deviation, gradually changing with the downstream development, can be observed in the non-equilibrium counterpart. This indicates the ongoing development of turbulent scales in the non-equilibrium region as the lower slopes at *x/D*=5 and *x/D*=10 show that the large velocity increments have not yet been produced.

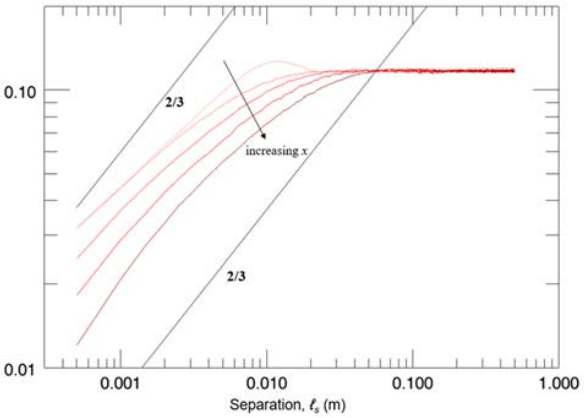

**Fig. 8:** Downstream development of second-order spatial structure functions along the jet centreline ($r = 0$). Each curve was shifted vertically for a clear comparison of the scales development. From *heavy to light red*: $x/D = 30$, 20, 15, 10, 5.

Furthermore, the second-order structure functions have significant spread at small separations closer to the jet exit and approach the same curve in the more downstream direction, which is consistent with the behavior of the spectra in the preceding section.

Fig. 9(a) – (e) show the spatial second-order structure functions along all measured radial positions, displaying one figure per measured downstream position. A similar bump is also noticed at the most upstream position as what has been seen in the corresponding spectra earlier. Most of the turbulent kinetic energy is dominated by the large scales in this position, as expected. Increasing large-scale activity is noticed in the outer part of the jet compared to on the centreline and the large scales are also observed to grow downstream.

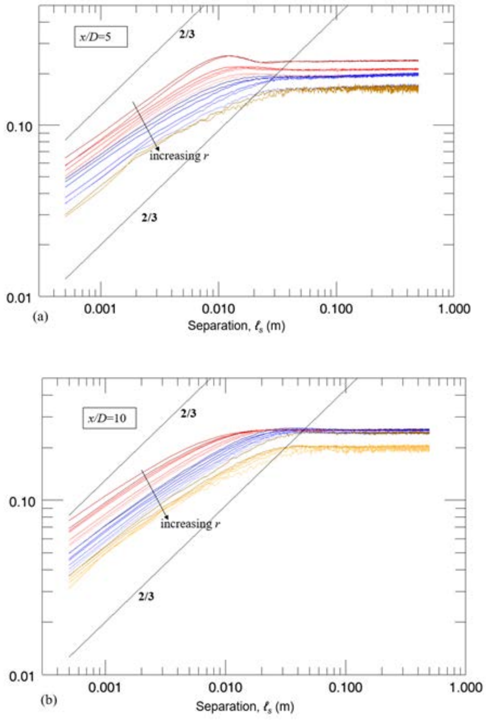

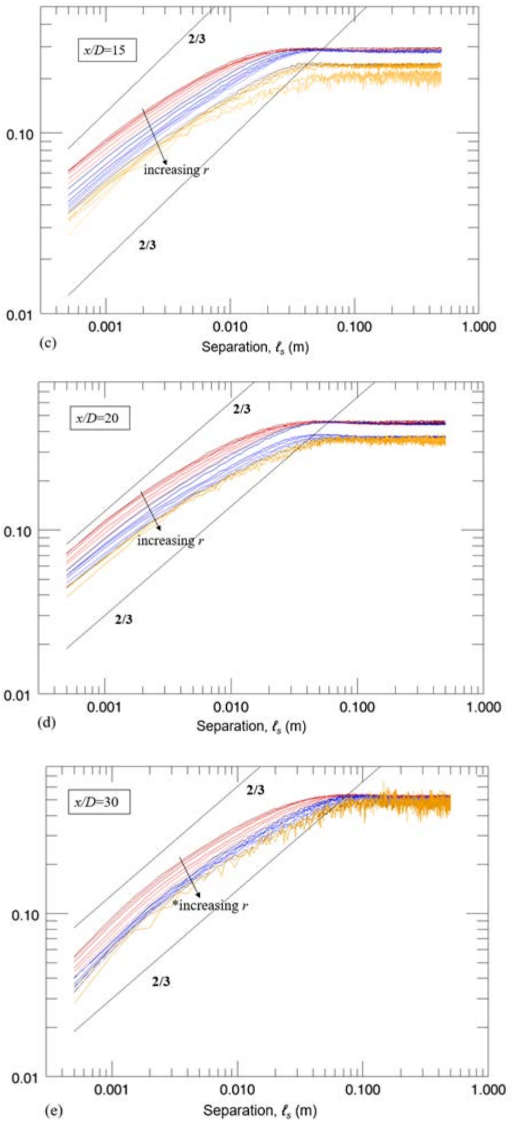

**Fig. 9:** Second-order spatial structure functions variations with radial distance at: (a) $x/D$=5. From *heavy to light red*: $r/D$ = 0, 0.1, 0.2, 0.3, 0.4, 0.5, 0.6. From *heavy to light blue*: $r/D$ = 0.7, 0.8, 0.9, 1, 1.1, 1.2. From *heavy to light brown*: $r/D$ = 1.3, 1.4. (b) x/D=10. From *heavy to light red*: $r/D$ = 0, 0.1, 0.2, 0.3, 0.4, 0.5, 0.6. From *heavy to light blue*: $r/D$ = 0.7, 0.8, 0.9, 1, 1.1, 1.2, 1.3. From *heavy to light brown*: $r/D$ = 1.4, 1.5, 1.6, 1.7, 1.8. (c) $x/D$=15. From *heavy to light red*: $r/D$ = 0, 0.15, 0.3, 0.45, 0.6, 0.75. From *heavy to light blue*: $r/D$ = 0.9, 1.05, 1.2, 1.35, 1.5, 1.65, 1.8. From *heavy to light brown*: r/D = 1.95, 2.1, 2.25, 2.4, 2.55, 2.7. (d) $x/D$=20. From *heavy to light red*: $r/D$ = 0, 0.2, 0.4, 0.6, 0.8, 1. From *heavy to light blue*: $r/D$ = 1.2, 1.4, 1.6, 1.8, 2, 2.2, 2.4. From *heavy to light brown*: $r/D$ = 2.6, 2.8, 3, 3.2. (e) $x/D$=30. From *heavy to light red*: $r/D$ = 0, 0.3, 0.6, 0.9, 1.2, 1.5. From *heavy to light blue*: $r/D$ = 1.8, 2.1, 2.4, 2.7, 3, 3.3, 3.6. From *heavy to light brown*: $r/D$ = 3.9, 4.2, 4.5. *Note that the arrow indicating the increment of radial distance, r, is not applicable for the two outermost points due to high variation in the plots. Each curve was shifted vertically for a clear comparison of the scales development.

### 3.4 Spatial third-order structure function

The third-order structure function is expected to follow Kolmogorov's 4/5 law only under these three assumptions, viz., the flow is locally in equilibrium, locally homogeneous and isotropic. We thereby present the third-order structure function as a function of spatial separation, $\ell$ at $x/D$=30 (see Fig. 10) where turbulence is evidenced to be fully developed based on the energy spectra presented earlier and also in [18)19)]. The results presented herein only cover up to the first six radial points including at the centreline due to due to high noise level towards the outermost region. For clear comparison to the Kolmogorov 4/5 law, a corresponding straight line constructed from Eq. 10 is also included in each plot, having the 4/5 slope. Note that the slope in this case is positive since the negative sign has been cancelled out by the negative value of the mean energy dissipation rate, $\varepsilon$. The structure function plots are observed to follow the 4/5 slope at the lower separation region, as expected. This finding also supports the simulation work done by [31)] where the 4/5 power law has been approximately indicated from an unforced turbulent flow. The third-order structure functions at $x/D$=20 are shown in Fig. 11 after we observed the positive tendency to follow the -5/3 slope to a certain extent of the wavenumber range based on the spectra in Fig. 7(c) previously.

An obvious advantage of plotting the spatial third-order structure function according to the assumptions of Kolmogorov[26)], is to be able to estimate , under the given assumptions, the mean energy dissipation rate per unit mass, $\varepsilon_{45}$. The parameter $\varepsilon$ from Eq. 10 was fine-tuned in the program for the 4/5 slope to best coincide at the small separations of the third-order structure function. This fit gave us the value of $\varepsilon_{45}$ at each measured position in the flow. The absolute values are then plotted in Fig. 12, which reveals that $\varepsilon_{45}$ drops substantially with increased radial distance from the jet centreline at $x/D$=20 but slowly at $x/D$=30. There is also a rapid drop along the centreline from $x/D$=20 to $x/D$=30, which further detailed investigation can be found in [32)].

Though the Kolmogorov 4/5 law is only valid for locally homogeneous flow, Eq. 10 has been naively employed to crudely estimate $\varepsilon_{45}$ in the non-equilibrium region. Repeating naively the same approach as implemented before, radial variation of $\varepsilon_{45}$ for $x/D$=10 and $x/D$=15 were determined and plotted in Fig. 13(a) together with those previously obtained for $x/D$=30 and $x/D$=20. The comparison reveals that the drop in the dissipation estimate, $\varepsilon_{45}$ is even more drastic in the more upstream positions. Surprisingly, the radial variation of $\varepsilon_{45}$ is also (relatively) consistent even at $x/D$=15 where the assumptions stated earlier clearly do not hold. Meanwhile, a sudden drop is observed along the radial direction at $x/D$=10, which certainly corresponds to the non-equilibrium region based on the spectra obtained in Fig. 8. Although these could not be credible regarding dissipation estimation, the third-order structure functions for $x/D$=15 and $x/D$=10 are nevertheless attached in Appendix II and III, respectively.

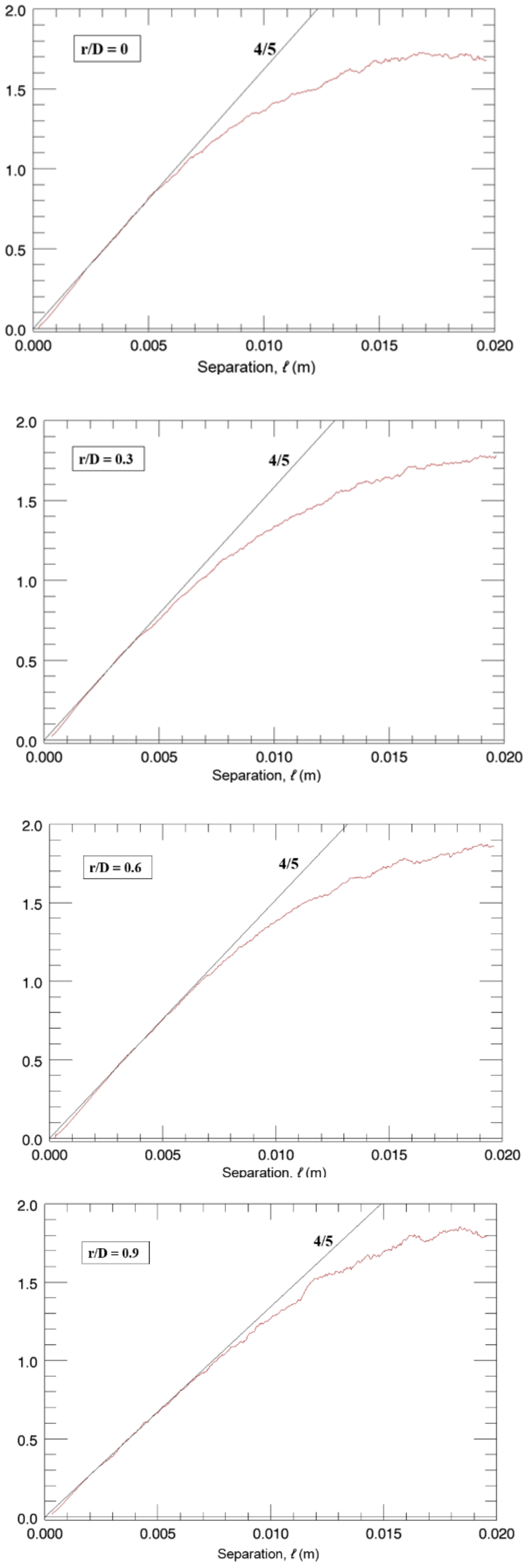

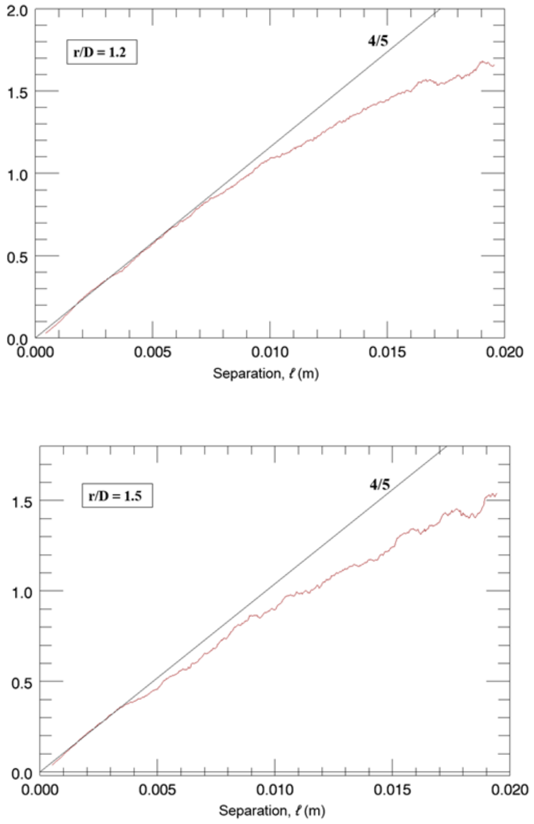

**Fig. 10:** Spatial third-order structure functions variations with radial distance at x/D=30. Due to high variations in the plots beyond r/D =1.5, only functions up this position are presented. Separate plots are made to clearly show the coincidence between each function and the 4/5 slope.

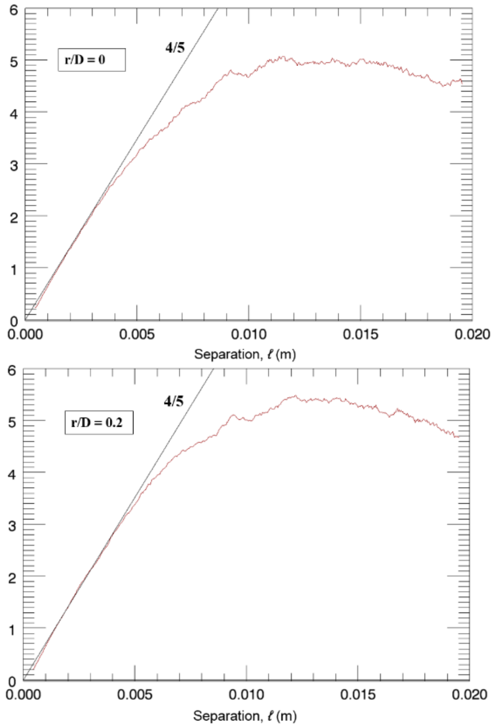

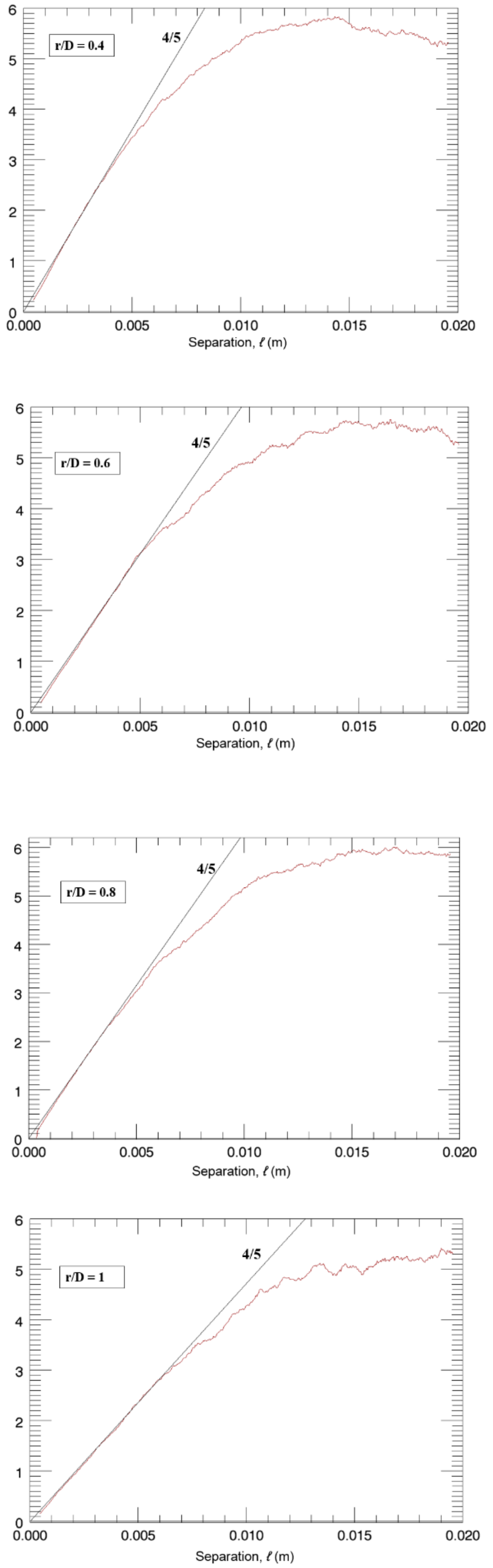

**Fig. 11:** Spatial third-order structure functions variations with radial distance at *x/D*=20. Due to high variations in the plots beyond *r/D* =1, only functions up this position are presented. Separate plots are made to clearly show the coincidence between each function and the 4/5 slope.

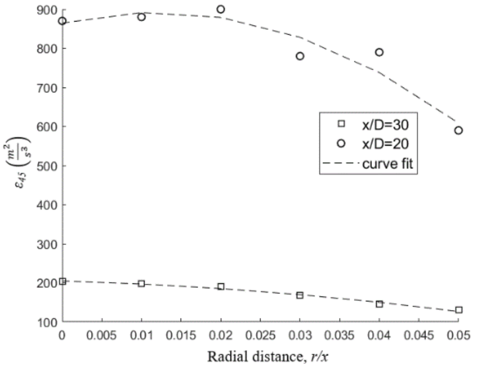

**Fig. 12:** Radial evolutions of $\varepsilon_{45}$ at *x/D*=30 and *x/D*=20, with second-order polynomial curve fits

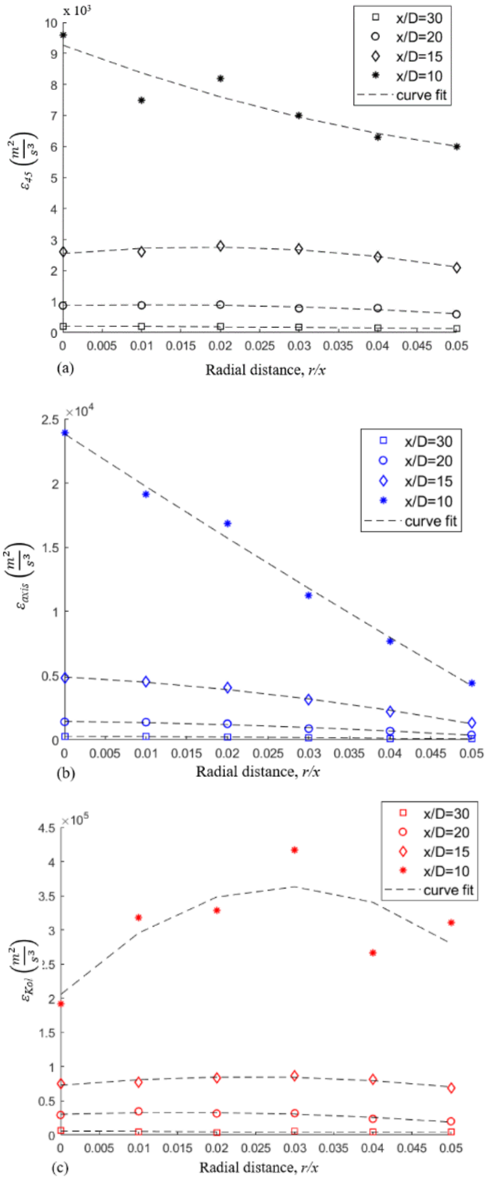

**Fig. 13:** Radial evolutions of (a) $\varepsilon_{45}$, (b) $\varepsilon_{axis}$ and (c) $\varepsilon_{Kol}$, with second-order polynomial curve fit

Besides $\varepsilon_{45}$, the dissipation based on the local axisymmetry, $\varepsilon_{axis}$ and Kolmogorov estimation, $\varepsilon_{Kol}$ are also computed and plotted in Fig. 13(b) and (c), respectively. The former is determined by reading the value of $2\varepsilon_{axis}\,(x - x_0)\,/\,u^3 \approx 0.7$ for the corresponding radial position $r/(x\text{-}x_0)$ of Figure 21 in [15] while the latter is computed by $\overline{u^3}/L_u$, where $L_u$ is the integral length scale. The value of $x_0$ is taken from another measurement along the jet centreline[32]. The dissipation radially evolves much more consistently in the fully developed region compared to the more upstream counterpart. Remarkably different trends are revealed at *x/D*=10 (developing region) between $\varepsilon_{45}$, for which the assumptions for 4/5 law are not fulfilled, and $\varepsilon_{Kol}$,, which are both central results from the same Kolmogorov theory. These two dissipation estimates should give (at least approximately) the same values AND consequently show similar trend if the theory and its underlying assumptions are correct and valid. It is also noteworthy, that ALL three estimates in Fig. 13 differ by order(s) of magnitude.

The spatial third-order structure functions for the other centreline positions i.e. at *x/D*=10 and *x/D*=15 are shown in Fig. 14(a) and (b), respectively. Observing the functions across different downstream distances, for instance at *r/D*=0, the tendency for the functions to follow the 4/5 slope is lower in the upstream direction. The break in the curves is observed also to occur at smaller $\ell$ as the measurement gets closer to the jet exit, which indicates that there are fewer large structures in the upstream region. The plot for *x/D*=5 is not shown, since we observe that the flow is still laminar in this position and therefore not possible to fit to the 4/5 slope.

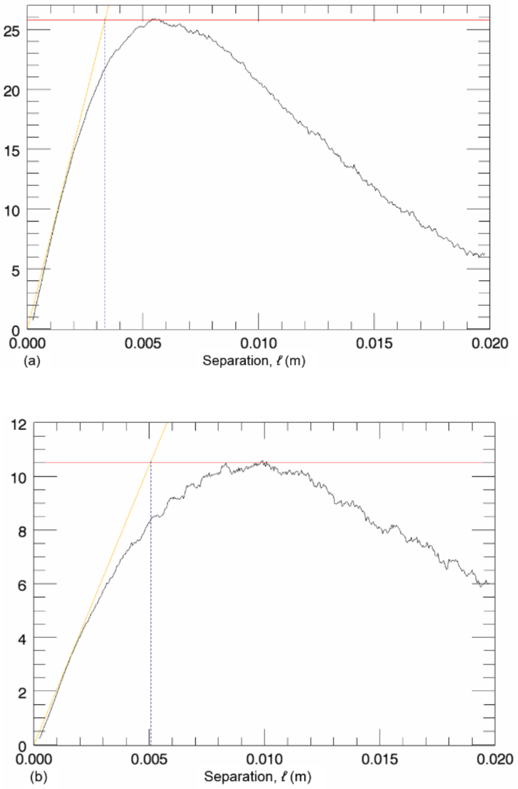

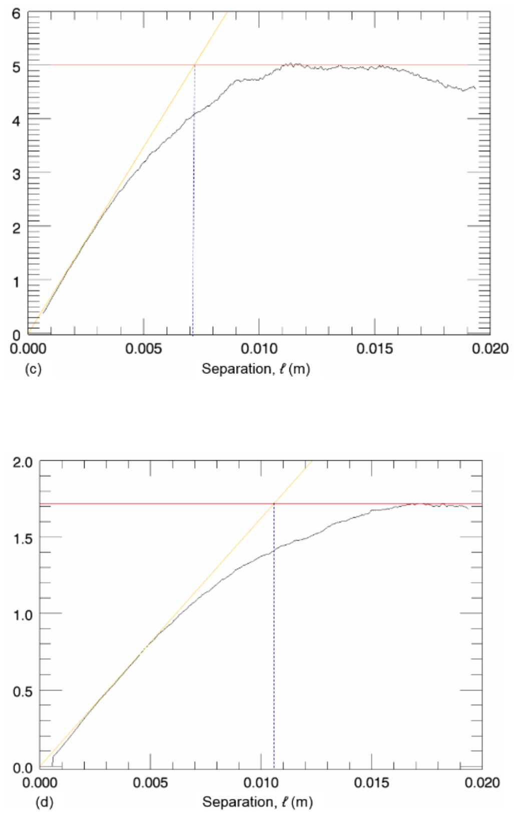

**Fig. 14:** Spatial third-order structure function at centreline for: a) *x/D*=10, b) *x/D*=15 c) *x/D*=20, d) *x/D*=30. The yellow and red lines represent the 4/5 slope and horizontal tangent line to each structure function curves, respectively, which intersection indicating the break point of the curve. The break occurs at approximately 3.354 mm, 5.041 mm, 7.16 mm and 10.6 mm at *x/D*=10, *x/D*=15, *x/D*=20 and *x/D*=30, respectively.

### 3.5 Turbulent scales

The values of dissipation extracted from the third-order structure function, $\varepsilon_{45}$, are used to determine the Kolmogorov time and length scales at *x/D*=20 and 30, which are plotted in Fig. 15. Both scales grow with a similar trend at each downstream position. The scales at *x/D*=30 are also larger than those at *x/D*=20. The Kolmogorov scales are also computed based on the axisymmetric dissipation, $\varepsilon_{\text{axis}}$, which values are overlaid in Fig. 15. This dissipation estimate is taken into account since it has been empirically established in [33)15)] and therefore considered as the most credible one.

The smallest resolvable length scale is also computed based on the size of measuring volume (MV) used in the measurements. From

$$k\eta_{Kol} = 1 \qquad (15)$$

at which the dissipation is approximately 99% resolved, the smallest resolvable scale using our instrument is calculated to be around $\lambda/2 \cdot 1/\pi$ = 28.6 μm. This value is represented by a horizontal blue line in Fig. 15, which is always way below the polynomial curve of the Kolmogorov length scales. It shows that, with the current spatial resolution used in our measurement setup, we should be able to resolve the Kolmogorov scale throughout this region, and perhaps in the upstream region since the blue line falls much lower than the estimated length scales.

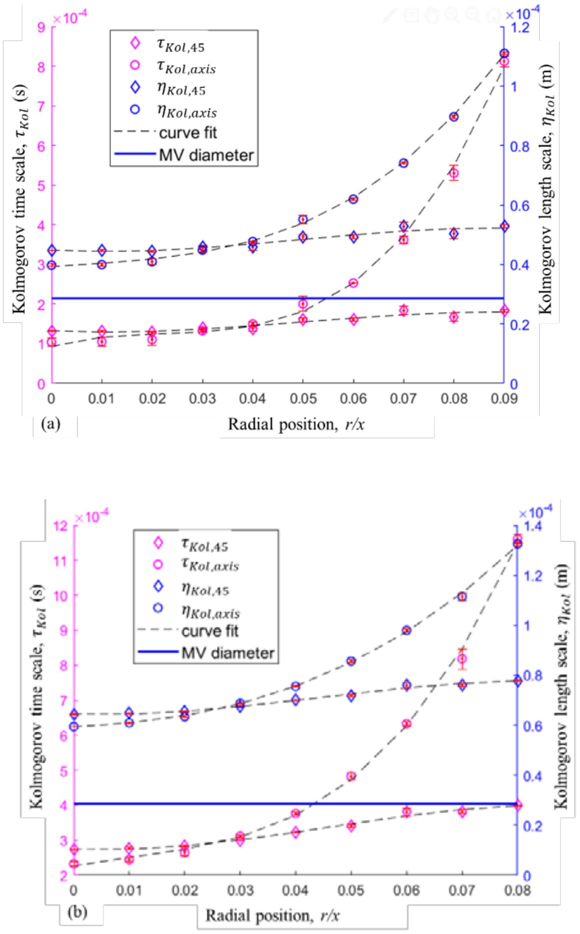

**Fig. 15:** Radial evolution of the Kolmogorov scales at (a) x/D=20, (b) x/D=30, with third-order polynomial fit. The blue horizontal line represents the smallest resolvable scale of our instrument, i.e., 28.6 μm, which is always below the polynomial curve of the Kolmogorov length scales

## 4. Conclusions

Both the static and dynamic first and second-order statistics of the streamwise velocity across the developing region of the round jet have been presented in the spatial domain. These statistics have been measured with an improved laser Doppler anemometry system (as compared to the limited commercially available systems). Due to the high dynamic range and ability to unambiguously distinguishing the velocity components, laser Doppler anemometry is the most suitable method to measure these high shear and high intensity flows.

It is observed that the first and second-order static moments can be collapsed across radial scans even down to approximately 15-20 jet exit diameters from the jet exit. Dynamic statistics mapping of the developing region, including across the radial dimension, has been presented in terms of spatial spectra as well as second- and third-order structure functions. The gradual development towards the Kolmogorov power laws (-5/3, 2/3 and 4/5, from the spatial spectra and second- and third-order structure functions, respectively) as one approaches the fully developed region is explicitly mapped. The - 5/3 law in the spectra and the 2/3 law in the second-order structure functions are approximated as early as 20 jet exit diameters downstream of the jet exit.

Although we only present (static and dynamic) statistics herein, the spectra and structure functions clearly witness that the round jet developing region cannot be in universal local equilibrium. Since they do not follow the classical -5/3 spectral and 2/3 second order structure function power laws, the predominating local transfer of energy in wavenumber space, as hypothesized by Richardson8), becomes questionable.

The measuring volume has been shown to be sufficiently small to capture scales of the order of the Kolmogorov length scale. Dissipation has been estimated using the 4/5 law based on the third-order structure functions, as well as based on the axisymmetric dissipation scaling of 15) and the classical zeroth law of turbulence epsilon$= u^3/L$. The corresponding Kolmogorov length and time scales have been mapped, displaying similar trends but with differences of order(s) of magnitude in the obtained scales.

## Acknowledgements

The support of Ministry of Education Malaysia is gratefully acknowledged. The authors also wish to acknowledge the generous support of Fabriksejer, Civilingeniør Louis Dreyer Myhrwold og hustru Janne Myhrwolds Fond (grant journal no. 13-M7-0039 and 15-M7-0031) and Reinholdt W. Jorck og Hustrus Fond (grant journal no. 13-J9-0026). Part of this work has been initially accepted and presented at the 7th Mechanical Engineering Research Day (MERD'20).

## References

1) C. Li, and K. Ito, "Performance evaluation of wind decontamination system by computational fluid dynamics," *Evergreen*, 1 (*2*) 12–17 (2014). doi:10.5109/1495158.
2) W.K. Yinn, H.M. Kamar, and N. Kamsah, "Effects of surgical staff turning motion on airflow distribution inside a hospital operating room," *Evergreen*, 6 (*1*) 52–58 (2019). doi:10.5109/2321008.
3) M.M. Takeyeldein, T.M. Lazim, N.A.R. Nik Mohd, I.S. Ishak, and E.A. Ali, "Wind turbine design using thin airfoil sd2030," *Evergreen*, 6 (*2*) 114–123 (2019). doi:10.5109/2321003.
4) A.M. Halawa, B. Elhadidi, and S. Yoshida, "Aerodynamic performance enhancement using active flow control on du96-w-180 wind turbine airfoil," *Evergreen*, 5 (*1*) 16–24 (2018). doi:10.5109/1929723.
5) A.N. Kolmogorov, "The local structure of turbulence in incompressible viscous fluid for very large reynolds numbers," *C. R. Akad. Sci. SSSR*, 30 9–13 (1941).
6) G.K. Batchelor, "The theory of homogeneous turbulence," Cambridge University Press, 1953.
7) W.K. George, "Reconsidering the ' local equilibrium ' hypothesis for small scale turbulence," *EDP Sci.*, 1–27 (2014).
8) L.F. Richardson, "Weather Prediction by Numerical Process," UK: Cambridge Univ. Press, 1922.
9) A. Tsinober, "An informal introduction to Turbulence," Kluwer Academic Publishers, 2001.
10) F. Anselmet, R.A. Antonia, and L. Danaila, "Turbulent flows and intermittency in laboratory experiments," *Planet. Space Sci.*, 49 (*12*) 1177–1191 (2001). doi:10.1016/S0032-0633(01)00059-9.
11) A.N. Kolmogorov, "A refinement of previous hypothesis concerning the local structure of turbulence in a viscous incompressible fluid at high reynolds number," *J. Fluid Mech.*, 13 82–85 (1962).
12) L. Danaila, F. Anselmet, and R.A. Antonia, "An overview of the effect of large-scale inhomogeneities on small-scale turbulence," *Phys. Fluids*, 14 (*7*) 2475–2484 (2002). doi:10.1063/1.1476300.
13) E.S. Oran, "Lecture Prize Talk: The Reactive Flow of Ideas," in: 66th Annu. Meet. APS Div. Fluid Dyn., 2013.
14) M.M. Gibson, "Spectra of turbulence at high reynolds number," *Nature*, 195 1281–1283 (1962).
15) H.J. Hussein, S.P. Capp, and W.K. George, "Velocity measurements in a high-reynolds-number, momentum-conserving, axisymmetric, turbulent jet," *J. Fluid Mech.*, 258 31–75 (1994).
16) C.M. Velte, W.K. George, and P. Buchhave, "Estimation of burst-mode lda power spectra," *Exp. Fluids*, 55 (*3*) 1674 (2014).
17) M.R. Yaacob, R.K. Schlander, P. Buchhave, and C.M. Velte, "Validation of improved laser Doppler

anemometer (LDA) based on the fully developed turbulent round jet," in: Symp. Electr. Mechatronics Appl. Sci., 2018: pp. 89–90.

18) P. Buchhave, and C.M. Velte, "Measurement of turbulent spatial structure and kinetic energy spectrum by exact temporal-to-spatial mapping," *Phys. Fluids*, 29 (*8*) (2017).
19) M.R. Yaacob, R. Schlander, P. Buchhave, and C.M. Velte, "Experimental evaluation of kolmogorov's -5/3 and 2/3 power laws in the developing turbulent round jet," *J. Adv. Res. Fluid Mech. Therm. Sci.*, 45 (*2*) 14–21 (2018).
20) N.A. Rahmat, A. Hagishima, N. Ikegaya, and J. Tanimoto, "Experimental study on effect of spires on the lateral nonuniformity of mean flow in a wind tunnel," *Evergreen*, 5 (*1*) 1–15 (2018). doi:10.5109/1929670.
21) A.M.M. Ismaiel, and S. Yoshida, "Study of turbulence intensity effect on the fatigue lifetime of wind turbines," *Evergreen*, 5 (*1*) 25–32 (2018). doi:10.5109/1929727.
22) O.M.A.M. Ibrahim, and S. Yoshida, "Experimental and numerical studies of a horizontal axis wind turbine performance over a steep 2d hill," *Evergreen*, 5 (*3*) 12–21 (2018). doi:10.5109/1957496.
23) D. Jung, "An investigation of the Reynolds-number dependence of the axisymmetric jet mixing layer using a 138 hot-wire probe and the POD," State University of New York, 2001.
24) M.R. Yaacob, R.K. Schlander, P. Buchhave, and C.M. Velte, "Mapping of turbulent round jet developing region using a constant temperature anemometer (cta)," *Malaysian J. Fundam. Appl. Sci.*, (*Special Issue on Natural Sciences and Mathematics (ESCon 2018)*) 443–446 (2018).
25) J.L. Lumley, "Interpretation of time spectra measured in high-intensity shear flows," *Phys. Fluids*, 8 (*6*) 1056–1062 (1965). doi:10.1063/1.1761355.
26) A.N. Kolmogorov, "Dissipation of energy in the locally isotropic turbulence," *Dokl. Akad. Nauk. SSSR*, 32 15–17 (1941).
27) M. Khashehchi, A. Ooi, J. Soria, and I. Marusic, "Evolution of the turbulent/non-turbulent interface of an axisymmetric turbulent jet," *Exp. Fluids*, 54 (*1*) 1449 (2013). doi:10.1007/s00348-012-1449-3.
28) I. Danaila, J. Dušek, and F. Anselmet, "Coherent structures in a round, spatially evolving, unforced, homogeneous jet at low reynolds numbers," *Phys. Fluids*, 9 (*11*) 3323–3342 (1997). doi:10.1063/1.869446.
29) E. Gutmark, "Preferred modes and the spreading rates of jets," *Phys. Fluids*, 26 (*10*) 2932 (1983). doi:10.1063/1.864058.
30) G.P. Romano, and R.A. Antonia, "Longitudinal and transverse structure functions in a turbulent round jet: effect of initial conditions and reynolds number," *J. Fluid Mech.*, 436 231–248 (2001). doi:10.1017/S0022112001003901.
31) O.N. Boratav, and R.B. Pelz, "Structures and structure functions in the inertial range of turbulence," *Phys. Fluids*, 9 (*5*) 1400–1415 (1997). doi:10.1063/1.869253.
32) M.R. Yaacob, P. Buchhave, and C.M. Velte, "Statistical description of the turbulent round jet developing region along its centerline," *J. Adv. Res. Fluid Mech. Therm. Sci.*, (*2*) 337–353 (2019).
33) W.K. George, and H.J. Hussein, "Locally axisymmetric turbulence," *J. Fluid Mech.*, 233 1–23 (1991).

## Appendix I

Coefficient values for polynomial profiles, e.g., $P(x)= C_5x^5 + C_4x^4 + C_3x^3 + C_2x^2 + C_1x + C_0$

**Fig. 3**

| Profiles | $x/D$ | $C_5$ | $C_4$ | $C_3$ | $C_2$ | $C_1$ | $C_0$ |
|---|---|---|---|---|---|---|---|
| $\bar{u}$ | 5 | 2.7043 | -31.5232 | 92.7324 | -99.05 | 12.6895 | 30.2185 |
| | 10 | -0.9914 | 2.7245 | 1.8098 | -7.8979 | -7.946 | 21.6883 |
| | 15 | -0.0344 | -0.4016 | 3.9716 | -9.4386 | 1.195 | 15.0599 |
| | 20 | 0.0459 | -0.5736 | 2.7533 | -5.7668 | 1.294 | 11.1633 |
| | 30 | 0.0085 | -0.1127 | 0.5881 | -1.3992 | -0.1950 | 7.5924 |
| $\overline{u^2}$ | 5 | -164.4077 | 657.5424 | -909.1178 | 459.1237 | -38.3987 | 11.2505 |
| | 10 | -12.1741 | 57.5851 | -89.7139 | 43.7588 | -5.1223 | 20.4405 |
| | 15 | -0.9391 | 6.7945 | -16.1307 | 11.5517 | -0.5859 | 10.8377 |
| | 20 | -0.1019 | 0.9497 | -2.72 | 1.5749 | 1.0260 | 6.4602 |
| | 30 | 0.0023 | -0.0084 | -0.0097 | -0.1677 | 0.3021 | 3.2004 |
| $\sqrt{\frac{\overline{u^2}}{\bar{u}^2}}$ | 5 | 139.3703 | -341.2986 | 261.6864 | -33.0136 | 13.5632 | 10.6128 |
| | 10 | 13.14 | -40.0016 | 41.8063 | -6.4274 | 11.9347 | 20.6575 |
| | 15 | 2.1464 | -9.3531 | 12.445 | 3.4893 | 2.4062 | 21.7319 |
| | 20 | 0.8674 | -4.8501 | 8.2393 | -0.0668 | 3.1112 | 22.6348 |
| | 30 | 0.1292 | -1.1715 | 3.5103 | -2.4894 | 4.6474 | 23.3794 |

**Fig. 4**

| Profiles | $x/D$ | $C_5$ | $C_4$ | $C_3$ | $C_2$ | $C_1$ | $C_0$ |
|---|---|---|---|---|---|---|---|
| $\sqrt{\frac{\overline{u^2}}{\bar{u}^2}}$<br>(normalized) | 10 | 1.314E6 | -4E5 | 4.1806E4 | -642.7418 | 119.3467 | 20.6575 |
| | 15 | 1.63E6 | -4.735E5 | 4.2002E4 | 785.0979 | 36.093 | 21.7319 |
| | 20 | 2.7756E6 | -7.7601E5 | 6.5914E4 | -26.7026 | 62.2235 | 22.6348 |
| | 30 | 3.1407E6 | -1.0379E6 | 1.173E5 | -4.0403E3 | 174.65 | 22.4991 |

| | | | | | | | |
|---|---|---|---|---|---|---|---|
| $\frac{\bar{u}}{U_C}$ | 10 | -4.5466E3 | 1.2494E3 | 82.9961 | -36.2184 | -3.6439 | 0.9946 |
| | 15 | -1.7303E3 | -1.3448E3 | 886.6266 | -140.4744 | 1.1857 | 0.9962 |
| | 20 | 1.3163E4 | -8.2202E3 | 1.973E3 | -206.6252 | 2.3181 | 1 |
| | 30 | 2.7306E4 | -1.2796E4 | 2.3731E3 | -203.8171 | 1.32 | 1 |
| $\frac{\overline{u^2}}{\overline{u^2}_C}$ | 10 | -5.8475E4 | 2.7659E4 | -4.3092E3 | 210.1828 | -2.4604 | 0.9818 |
| | 15 | -6.5205E4 | 3.3625E4 | -5.8456E3 | 345.7944 | -4.6739 | 1.0084 |
| | 20 | -5.0687E4 | 2.4884E4 | -3.867E3 | 152.2504 | 1.9446 | 0.9910 |
| | 30 | 1.7747E4 | -3.5952E3 | 108.8738 | -47.2045 | 4.3604 | 0.9353 |

**Fig. 12**

| Profiles | *x/D* | $C_5$ | $C_4$ | $C_3$ | $C_2$ | $C_1$ | $C_0$ |
|---|---|---|---|---|---|---|---|
| $\varepsilon_{45}$ | 20 | N/A | N/A | N/A | -1.9464E5 | 4.6179E3 | 864.6429 |
| | 30 | N/A | N/A | N/A | -1.9643E4 | -577.8571 | 204.7857 |

**Fig. 13**

| Profiles | *x/D* | $C_5$ | $C_4$ | $C_3$ | $C_2$ | $C_1$ | $C_0$ |
|---|---|---|---|---|---|---|---|
| $\varepsilon_{45}$ | 10 | N/A | N/A | N/A | 6.0714E5 | -9.55E4 | 9.2643E3 |
| | 15 | N/A | N/A | N/A | -6.3393E5 | 2.2982E4 | 2.5482E3 |
| | 20 | N/A | N/A | N/A | -1.9464E5 | 4.6179E3 | 864.6429 |
| | 30 | N/A | N/A | N/A | -1.9643E4 | -577.8571 | 204.7857 |
| $\varepsilon_{axis}$ | 10 | N/A | N/A | N/A | 5.2797E6 | -4.9709E6 | 2.8588E5 |
| | 15 | N/A | N/A | N/A | -7.8928E5 | -3.3403E4 | 4.8936E3 |
| | 20 | N/A | N/A | N/A | -2.8703E5 | -7.2421E3 | 1.4316E3 |
| | 30 | N/A | N/A | N/A | -2.1889E4 | -3.4142E3 | 285.1434 |

| | | | | | | | |
|---|---|---|---|---|---|---|---|
| $\varepsilon_{Kol}$ | 10 | N/A | N/A | N/A | -2.82E8 | 1.6342E7 | 3.0801E5 |
| | 15 | N/A | N/A | N/A | -2.1393E7 | 1.024E6 | 7.2855E4 |
| | 20 | N/A | N/A | N/A | -1.165E7 | 3.5573E5 | 3.0383E4 |
| | 30 | N/A | N/A | N/A | 1.4792E6 | -9.439E4 | 6.0981E3 |

**Fig. 15**

| *x/D* | Profiles | $C_5$ | $C_4$ | $C_3$ | $C_2$ | $C_1$ | $C_0$ |
|---|---|---|---|---|---|---|---|
| 20 | $\tau_{Kol,45}$ | N/A | N/A | -0.2202 | 0.0329 | -6.495E-4 | 1.3274E-4 |
| | $\eta_{Kol,45}$ | N/A | N/A | -0.03552 | 0.005231 | -1.0113E-4 | 4.4833E-5 |
| | $\tau_{Kol,axis}$ | N/A | N/A | 2.0677 | -0.1375 | 0.003461 | 9.3416E-5 |
| | $\eta_{Kol,axis}$ | N/A | N/A | 0.1001 | -0.0015 | 1.1587E-4 | 3.9277E-5 |
| 30 | $\tau_{Kol,45}$ | N/A | N/A | -0.5103 | 0.0696 | -7.5205E-4 | 2.7469E-4 |
| | $\eta_{Kol,45}$ | N/A | N/A | -0.0564 | 0.007477 | -7.2468E-5 | 6.4493E-5 |
| | $\tau_{Kol,axis}$ | N/A | N/A | 2.236 | -0.07126 | 0.002889 | 2.2652E-4 |
| | $\eta_{Kol,axis}$ | N/A | N/A | 0.0584 | 0.005458 | 9.6858E-5 | 5.9252E-5 |

**Fig. 16**

| Profiles | *x/D* | $C_5$ | $C_4$ | $C_3$ | $C_2$ | $C_1$ | $C_0$ |
|---|---|---|---|---|---|---|---|
| $T_u$ | 10 | 13.6903 | -9.4634 | 1.8048 | -0.1456 | 0.004974 | 1.3484E-4 |
| | 15 | 160.7938 | -53.233 | 4.7839 | -0.04375 | -0.004535 | 4.6798E-4 |
| | 20 | 262.2984 | -86.1051 | 8.8756 | -0.3633 | 0.01041 | 6.1142E-4 |
| | 30 | 820.8543 | -311.4520 | 40.8385 | -2.2913 | 0.05511 | 0.001333 |
| $L_u$ | 10 | 284.1285 | -196.4038 | 37.4568 | -3.0214 | 0.1032 | 0.002798 |
| | 15 | 2305.0438 | -763.1165 | 68.5785 | -0.6272 | -0.065 | 0.006709 |
| | 20 | 2854.0885 | -936.9162 | 96.5765 | -3.9534 | 0.1132 | 0.006653 |
| | 30 | 5905.4256 | -2240.6618 | 293.8023 | -16.4842 | 0.3965 | 0.009592 |

## Appendix II

Spatial third order structure function plots at *x/D*=15

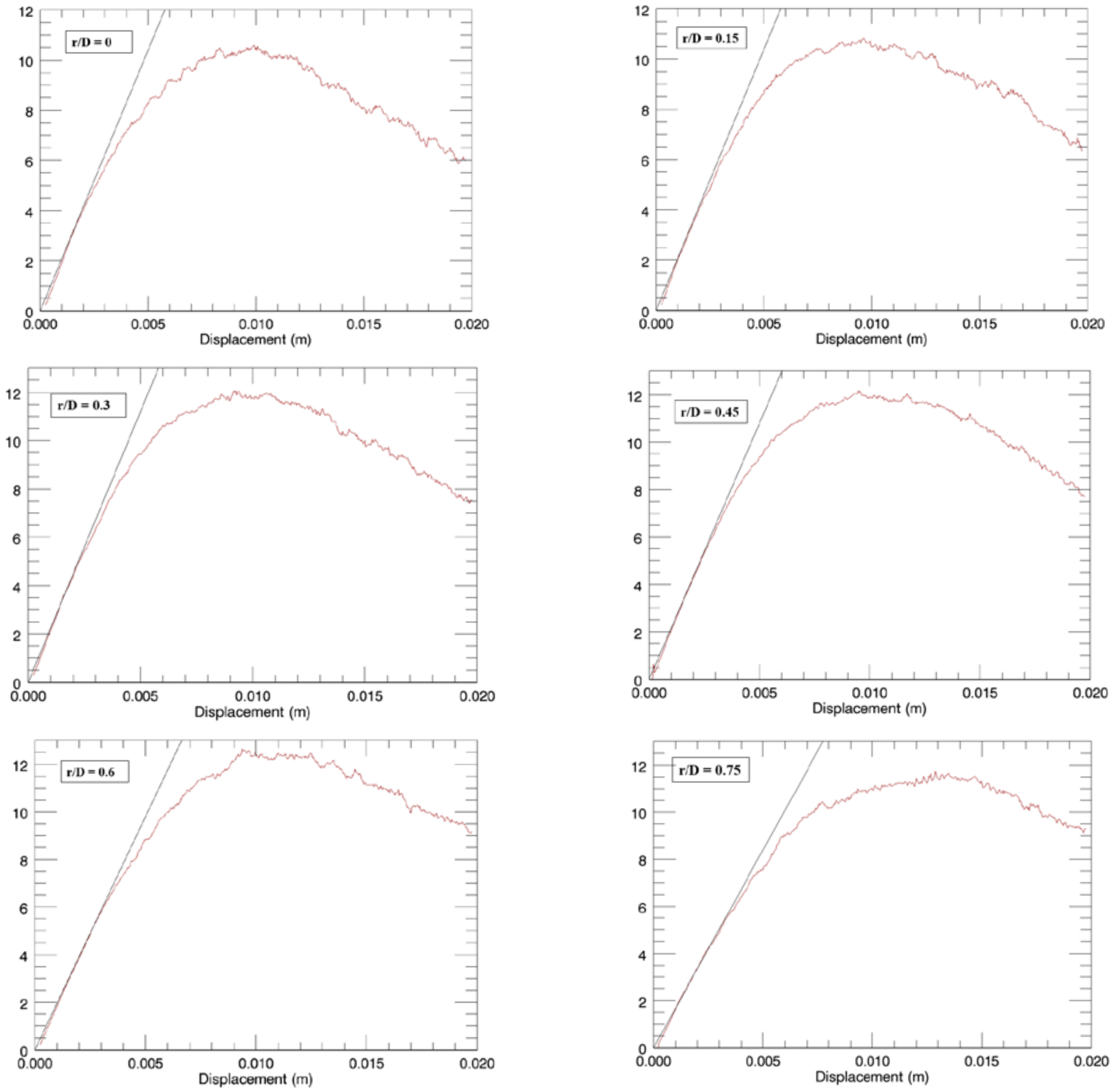

## Appendix III

Spatial third order structure function plots at *x/D*=10